Matter and Radiation at Extremes

RESEARCH ARTICLE | OCTOBER 23 2025

Demonstration of full-scale spatiotemporal diagnostics of solid-density plasmas driven by an ultra-short relativistic laser pulse using an X-ray free-electron laser

Special Collection: Special Issue on ICMRE2024

Lingen Huang ✉ ; Michal Šmíd ; Long Yang ; Oliver Humphries ; Johannes Hagemann ; Thea Engler ; Xiayun Pan ; Yangzhe Cui ; Thomas Kluge ; Ritz Aguilar ; Carsten Baehtz ; Erik Brambrink ; Engin Eren ; Katerina Falk ; Alejandro Laso Garcia ; Sebastian Göde; Christian Gutt ; Mohamed Hassan ; Philipp Heuser ; Hauke Höppner ; Michaela Kozlova ; Wei Lu ; Josefine Metzkes-Ng ; Masruri Masruri ; Mikhail Mishchenko ; Motoaki Nakatsutsumi ; Masato Ota ; Özgül Öztürk ; Alexander Pelka ; Irene Prencipe ; Thomas R. Preston ; Lisa Randolph ; Martin Rehwald ; Hans-Peter Schlenvoigt ; Ulrich Schramm ; Jan-Patrick Schwinkendorf ; Sebastian Starke ; Radka Štefaníková ; Erik Thiessenhusen; Monika Toncian ; Toma Toncian ; Jan Vorberger ; Ulf Zastrau ; Karl Zeil ; Thomas E. Cowan

Matter Radiat. Extremes 11, 017201 (2026)
https://doi.org/10.1063/5.0279974

Matter and Radiation at Extremes | RESEARCH ARTICLE | pubs.aip.org/aip/mre

Demonstration of full-scale spatiotemporal diagnostics of solid-density plasmas driven by an ultra-short relativistic laser pulse using an X-ray free-electron laser

Cite as: Matter Radiat. Extremes 11, 017201 (2026); doi: 10.1063/5.0279974
Submitted: 9 May 2025 • Accepted: 29 September 2025 •
Published Online: 23 October 2025

Lingen Huang,[1,a)] Michal Šmíd,[1] Long Yang,[1,2] Oliver Humphries,[3] Johannes Hagemann,[4] Thea Engler,[4] Xiayun Pan,[1,2] Yangzhe Cui,[1] Thomas Kluge,[1] Ritz Aguilar,[1] Carsten Baehtz,[1] Erik Brambrink,[3] Engin Eren,[5] Katerina Falk,[1] Alejandro Laso Garcia,[1] Sebastian Göde,[3] Christian Gutt,[6] Mohamed Hassan,[1] Philipp Heuser,[5] Hauke Höppner,[1] Michaela Kozlova,[1,7] Wei Lu,[3] Josefine Metzkes-Ng,[1] Masruri Masruri,[1] Mikhail Mishchenko,[3] Motoaki Nakatsutsumi,[3] Masato Ota,[8] Özgül Öztürk,[6] Alexander Pelka,[1] Irene Prencipe,[1] Thomas R. Preston,[3] Lisa Randolph,[3] Martin Rehwald,[1] Hans-Peter Schlenvoigt,[1] Ulrich Schramm,[1,2] Jan-Patrick Schwinkendorf,[3] Sebastian Starke,[1] Radka Štefaníková,[1,2] Erik Thiessenhusen,[1] Monika Toncian,[1] Toma Toncian,[1] Jan Vorberger,[1] Ulf Zastrau,[3] Karl Zeil,[1] and Thomas E. Cowan[1,2]

AFFILIATIONS

[1] Helmholtz-Zentrum Dresden-Rossendorf, 01328 Dresden, Germany
[2] Technische Universität Dresden, 01062 Dresden, Germany
[3] European XFEL, 22869 Schenefeld, Germany
[4] Center for X-Ray and Nano Science CXNS, Deutsches Elektronen-Synchrotron DESY, Notkestraße 85, 22607 Hamburg, Germany
[5] Helmholtz Imaging, Deutsches Elektronen-Synchrotron DESY, 22607 Hamburg, Germany
[6] Universität Siegen, 57072 Siegen, Germany
[7] ELI Beamlines Facility, Za radnici 835, 25241 Dolni Brezany, Czech Republic
[8] National Institute for Fusion Sciences, 509-5292 Toki, Japan

Note: This paper is part of the Special Issue on the 7th International Conference on Matter and Radiation at Extremes (ICMRE2024).
[a)] **Author to whom correspondence should be addressed:** lingen.huang@hzdr.de

ABSTRACT

Understanding the complex plasma dynamics in ultra-intense relativistic laser–solid interactions is of fundamental importance for applications of laser–plasma-based particle accelerators, the creation of high-energy-density matter, understanding planetary science, and laser-driven fusion energy. However, experimental efforts in this regime have been limited by the lack of accessibility of over-critical densities and the poor spatiotemporal resolution of conventional diagnostics. Over the last decade, the advent of femtosecond brilliant hard X-ray free-electron lasers (XFELs) has opened new horizons to overcome these limitations. Here, for the first time, we present full-scale spatiotemporal measurements of solid-density plasma dynamics, including preplasma generation with tens of nanometer scale length driven by the leading edge of a relativistic laser pulse, ultrafast heating and ionization at the main pulse arrival, the laser-driven blast wave, and transient surface return current-induced compression dynamics up to hundreds of picoseconds after interaction. These observations are enabled by utilizing a novel combination of advanced X-ray diagnostics including small-angle X-ray scattering, resonant X-ray emission spectroscopy, and propagation-based X-ray phase-contrast imaging simultaneously at the European XFEL-HED beamline station.

 https://doi.org/10.1063/5.0279974

I. INTRODUCTION

When a solid target is irradiated by an ultra-short relativistic laser pulse with peak intensity of the order of 10^{20} W/cm^2, a copious number of electrons within a few nanometers skin depth are promptly ionized and accelerated up to few tens of MeV kinetic energy. The relativistic electrons then propagate ballistically into the solid target with a large current density of the order of 10^{13} A/cm^2, depending on the laser absorption.[1] It is well known that the laser absorption during the arrival of the relativistic laser peak is critically determined by the surface density profile of the preplasma caused by the intrinsic laser rising edge or the prepulse, a few tens of picoseconds before the peak of the pulse is reached.[2,3] Although numerous studies have been conducted to measure the absolute laser absorption efficiency and its correlation with the scaling of generated hot-electron temperature,[4–7] it is still challenging to directly probe the density gradient of the preplasma, owing to its small spatial scale. The transport of hot electrons through the solid target further triggers plasma dynamic effects such as isochoric heating and ionization, development of kinetic instabilities, generation of extreme fields, radiation sources, and warm/hot dense plasmas. Moreover, after the main laser pulse reaches the target surface, hydrodynamic processes of shock generation, heat diffusion, magnetic Z-pinch and thermal pressure-driven compression, and magnetohydrodynamic instabilities occur over few-picosecond to sub-nanosecond timescales. Toward understanding the underlying physics of electron transport, tremendous effort has been dedicated over the last few decades to the examination of these complex phenomena via a variety of diagnostics, including optical shadowgraphy,[8] charged particle imaging,[9,10] X-ray radiography,[11] X-ray emission spectroscopy,[12] and X-ray Thomson scattering (XRTS).[13] However, these diagnostics are limited by inaccessibility to solid density, harsh bremsstrahlung background noise, or insufficient temporal and small spatial scales. Therefore, numerical approaches that can be more readily interrogated and performed at scale, such as magnetohydrodynamics (MHD) and particle-in-cell (PIC) simulations, play a key role in acquiring a fundamental understanding of the complex plasma dynamics involved.[14,15] Given the need for precise manipulation and control of high-intensity laser–solid interactions for potential applications such as cancer therapy via compact plasma-based particle accelerators[16] and laser-driven fusion energy,[17,18] it is highly desirable to develop novel diagnostics to overcome the above-mentioned limitations, and thus benchmark and strengthen the predictive power of numerical simulations.

The advent of novel experimental platforms equipped with both optical high-power lasers and ultra-short brilliant X-ray free-electron lasers (XFELs), such as the European XFEL-HED,[19] LCLS-MEC,[20] and SACLA beamline,[21] provides unprecedented opportunities for experimental studies of solid-density plasmas. State-of-the-art X-ray sources with an extremely high photon number per pulse (of the order of 10^{12}) and ultra-short duration (tens of femtoseconds) and wavelength (0.5 Å), and exhibiting nearly full transverse coherence, enables probing of the surface and internal structures of such overdense plasmas via scattering, diffraction, and absorption imaging, as well as spectroscopic methods at femtosecond and nanometer resolution simultaneously utilizing a single shot. The recent pioneering work conducted at the current hard XFEL facilities combining femtosecond high power lasers using the X-ray diagnostics of small angle X-ray scattering (SAXS),[22–24] grazing incidence SAXS (GISAXS),[25,26] X-ray phase contrast imaging (XPCI),[27–30] absorption imaging[31,32] and XRTS[33] clearly demonstrate the excellent capabilities.

Here, combining the cutting-edge diagnostics of SAXS, XPCI, and resonant X-ray emission spectroscopy (RXES), for the first time we are able to probe the complex dynamics of electron transport in relativistic laser–solid interactions in a multiscale spatiotemporal regime ranging from a few nanometers up to micrometers and a few tens of femtoseconds to hundreds of picoseconds. A pump–probe experiment was performed at the European XFEL-HED station, using the ReLaX high-intensity laser, with peak intensity up to 5×10^{20} W/cm^2, irradiating 10–25 μm diameter Cu and other wires probed by a femtosecond brilliant hard XFEL. While SAXS profiles are correlated with the nanometer pre-plasma scale length generated by a ~100 ps laser prepulse (Fig. 1), XPCI has been shown to be sensitive to density gradients from the sub-micrometer scale, enabling it to probe hydrodynamic evolution and instabilities, thermal expansion, and shock compression on the tens of picoseconds to sub-nanosecond timescale, thereby being able to reconstruct laser-driven blast waves and surface return current-induced dynamics.[30]

In conjunction, time-resolved resonant X-ray emission spectroscopy (RXES) was used to probe the plasma heating and ionization during the main pulse interaction. Fluorescence X-ray emission spectroscopy (XES) has frequently been used to infer plasma conditions from the intensity and ratio of characteristic X-ray lines,[34] but, owing to the femtosecond timescale evolution of dense plasmas driven by ultra-intense lasers, spectroscopic data are usually time-integrated, with X-ray streak cameras limited to ~1 ps temporal resolution.[35] XFELs provide unprecedented temporal resolution to probe laser-produced transient extreme states, limited by the XFEL pulse duration and the timing stability (femtoseconds to a few tens of femtoseconds).[19,36] By tuning the XFEL to be resonant with the K–L transition of nitrogen-like Cu^{22+} ions, pumped by the optical laser, the experimentally observed enhancement in XFEL beam attenuation and resonant X-ray emission provides a direct indication of the population of the selected ionization state. This reveals the underlying heating, ionization, and recombination dynamics, serving as a valuable benchmark for validating collisional and ionization models in solid-density plasmas.[14,23,37] An amalgam of these diagnostics—SAXS, XPCI, and RXES—is shown for the case of a Cu wire to enable simultaneous characterization of multiscale physics and electron transport through solid-density laser plasmas, as well as providing an important benchmark of the quality of the data that can be generated at modern X-ray light sources.

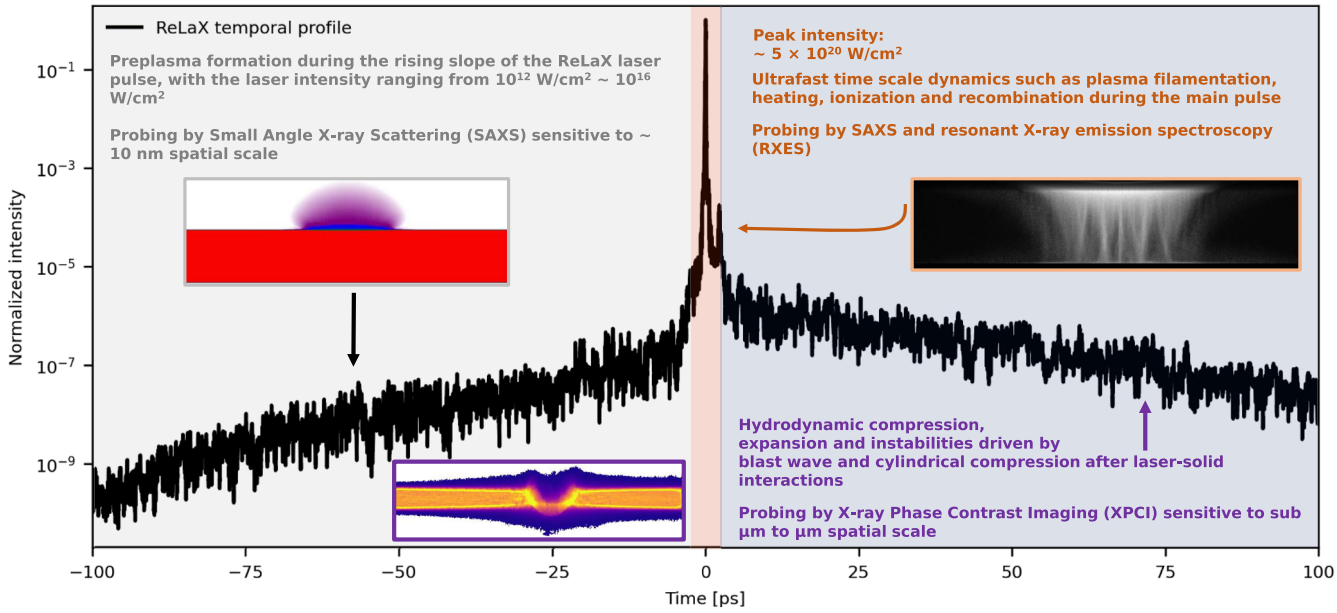

FIG. 1. Schematic of multiscale spatiotemporal plasma processes induced by electron transport in solid-density plasmas irradiated by ultra-short relativistic laser pulses, along with the corresponding X-ray diagnostics used in the pump–probe experiment. The black curve shows the realistic temporal profile of the ReLaX laser pulse ranging from −100 to 100 ps. Illustrations of preplasma formation, electron filamentation, blast wave, and compression, as predicted by our previous simulations,[14,15] are also shown.

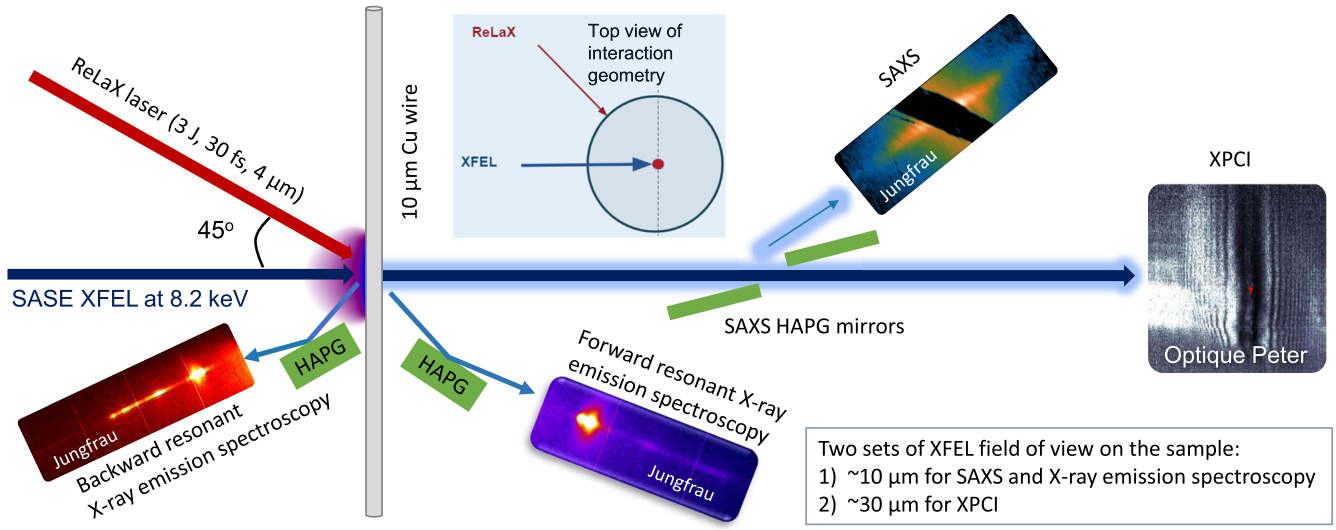

FIG. 2. Schematic of experimental setup. Both the optical relativistic ReLaX laser and the XFEL irradiate a Cu wire of 10 μm diameter at normal incidence, polarized in the horizontal direction. The ReLaX and X-ray beams intersect at an angle of 45°. The SAXS patterns and emission spectroscopy are recorded by the Jungfrau X-ray detectors. Two HAPG chromatic mirrors with a small gap are used to reflect the SAXS signal, allowing propagation of the primary XFEL beam to an Andor Zyla CMOS camera via a 7.5× objective for simultaneous XPCI imaging. The X-ray propagation distances from the sample to the SAXS and XPCI detectors are 1.31 and 6.31 m, respectively. The entire setup except for the SAXS Jungfrau detector and the last 50 cm before the Zyla detector is placed in vacuum conditions to minimize air scattering. The SAXS/RXES and XPCI data presented in this study correspond to the small FoV and large FoV on the wires of ~10 and ~30 μm respectively, which is achieved by switching two sets of compound refractive lens (CRL) configurations as described in the text.

II. EXPERIMENTAL SETUP

The pump–probe experiment was performed at the HED endstation at the European XFEL, with the ultra-intense optical laser facility ReLaX, a 3 J, 30 fs, 10 Hz Ti:sapphire-based system,[38] being used to create solid-density plasmas. A schematic illustration of the experimental setup is shown in Fig. 2. The ReLaX laser was focused to a full width at half maximum (FWHM) spot size of ~4 μm measured by the In Line Microscope (ILM) diagnostics with 20× microscope objective, resulting in a peak intensity up to 5×10^{20} W/cm^2 irradiating 10 μm Cu wires at normal incidence. The temporal contrast of pulse intensity shown in Fig. 1 was measured by the offline diagnostics package consisting of single-shot temporal pulse diagnostics, a scanning third-order intensity autocorrelator, and a spatial phase sensor in combination with a full-beam adaptive deformable mirror.[38] Note that the peak intensity has been obtained under the assumption that ReLaX has Gaussian profiles in both space and time. However, the actual laser focus deviates from a perfect Gaussian, with a significant amount of energy distributed outside the central region. A statistical analysis shows mean FWHM focal sizes of 3.9 μm (horizontal) and 3.6 μm (vertical) in the center, with relative standard deviations of 12% and 11%, respectively. The fraction of energy contained within the main focus is 0.44, with a relative standard deviation of 9%. Fluctuations in laser energy and pulse duration are very low and thus negligible compared with other sources. Combining all of these factors yields a relative intensity fluctuation of less than 25%.

The XFEL beam generated by the principle of self-amplified spontaneous emission (SASE) with an energy of ~1.5 mJ, an FWHM pulse duration of ~25 fs, and a photon energy centered at 8.2 keV with a FWHM bandwidth of ~20 eV, was used to probe the solid-density plasmas, aided by a combination of multiple X-ray diagnostics, including both imaging and spectroscopy, such as SAXS, RXES, and XPCI, simultaneously. The online calibrated High Resolution Hard X-ray Single-Shot (HIREX) spectrometer installed in the photon tunnel of the SASE2 undulator beamline was used to monitor the SASE spectrum,[39] ensuring the central X-ray photon energy remained fixed at 8.2 keV during the entire beamtime. The photon energy was cross-checked by the elastic X-ray scattering signal on Cu samples measured by a von Hámos X-ray spectrometer inside the interaction chamber.[40] The X-ray pulse energy was measured via an X-ray gas monitor (XGM) located in the photon tunnel and an intensity and position monitor (IPM) installed at the HED instrument.[19] Energy calibration of the IPM was performed during the preparation for the hot shots each beamtime shift.

Two sets of X-ray compound refractive lens (CRL) configurations were used to achieve the small and large fields of view (FoV) on the sample that are preferred for the SAXS/RXES and XPCI diagnostics, respectively. In the case of small FoV, arms 3, 6, and 10 of CRL3 (located in the HED optics hutch at ~962 m from the source[19]) were set to obtain a FWHM spot size of ~10 μm on the sample. In the case of a large FoV, arms 4 and 6 of CRL3 were used to achieve an FWHM spot size of ~30 μm on the sample. The XFEL focal spot size was characterized by edge scans of test samples via X-ray transmission imaging, using a GAGG scintillator-based detector (Optique Peter) coupled to an Andor Zyla CMOS camera equipped with a 7.5× objective lens, positioned 6.31 m downstream from the target chamber center. Two highly annealed pyrolytic graphite (HAPG) mirrors located symmetrically below and above the propagation path of the XFEL beam were used to reflect the SAXS signal to the Jungfrau X-ray detector.[41] Simultaneously, the XFEL beam passing through the gap between the HAPG mirrors was recorded by an Optique Peter instrument for XPCI imaging.[42]

The timing and synchronization between the optical and X-ray lasers was measured by an HED optical en-coding spatial photon arrival monitor (PAM).[43] The timing window measurable by the PAM was within 200 fs, giving the upper limit of the uncertainty of XFEL probe time delay relative to the ReLaX laser presented in this work.

III. EXPERIMENTAL RESULTS AND DISCUSSION

In this section, we present the details of each plasma diagnostic in turn: nanometer scale-sensitive SAXS, charge state-sensitive RXES, and sub-micrometer scale-sensitive XPCI to fully investigate the integrated spatiotemporal dynamics of solid-density plasmas driven by the ultra-intense ReLaX laser pulse. These diagnostics probe a range of spatiotemporal scales, including the preplasma generation with tens of nanometer-scale length driven by the leading edge of the ReLaX laser pulse, ultra-fast heating and ionization at the main pulse arrival, direct laser-driven blast wave, and the cylindrical pinch dynamics driven by the thermal ablative shock induced by the transient surface return current, up to hundreds of picoseconds after interaction.

A. SAXS measurements of preplasma expansion

Small-angle X-ray scattering arises from coherent superposition of elastic X-ray scattering in a given direction—usually considered as <1°. This direction is determined by the momentum transfer $\vec{q} = \vec{k} - \vec{k}'$, where $\vec{k}$ and $\vec{k}'$ are the incoming and scattering wave vectors, respectively. The SAXS intensity $I(\vec{q})$ is proportional to the spatial Fourier transform of the electron density n_e projected in the X-ray beam direction assuming homogeneous irradiation, as derived in previous theoretical work:[44,45]

$$I(q) = I_0 |\mathrm{FT}\{n_e\}|^2, \tag{1}$$

where I_0 is a constant factor depending on the initial incident X-ray fluence and the solid angle of the SAXS detector. Here, we assume that the projected density n_e is the convolution of the form, structure, and expansion terms that represent the averaged geometrical shape, individual electron–electron correlations, and sharpness of the wire edge, respectively, and so Eq. (1) can be rewritten as

$$I(\vec{q}) = I_0 F(\vec{q}) S(\vec{q}) E(\vec{q}), \tag{2}$$

where $F(\vec{q})$, $S(\vec{q})$, and $E(\vec{q})$ are the form, structure and expansion factors, respectively, in reciprocal or momentum space. In our SAXS setup, the momentum transfer q ranges from 0.08 to 0.45 nm^{-1}, indicating that SAXS is able to measure the scale length of the correlation structure from 5 to 100 nm. In this q range of interest, the form factor of a wire is approximately equal to $F(q) \simeq 1/q^3$ according to Porod's law.[46,47] For a cold wire with infinitely sharp density gradient between the edge of the target and the surrounding vacuum (a Heaviside step function), the SAXS pattern exhibits a strong streak feature parallel to the surface normal direction, with the intensity proportional to the dominant form factor, $I(q) \propto F(q)$. When

the wire is irradiated by the rising slope ranging from a few tens of picoseconds to 1 ps before the arrival of the peak ReLaX laser pulse, corresponding to the laser intensity rising from ~10^{13} to 10^{16} W/cm^2 as seen in Fig. 1, the scattering edge is smoothed by the preplasma expansion without bending by the hole boring process. Assuming the edge shape of wire radial density to be an error function $\mathrm{erf}\,(r/\sqrt{2}\sigma)$ with a finite scale length of σ, the expansion factor can be derived[22] as $E(q) = e^{-q^2\sigma^2}$. As the laser intensity is far below the relativistic intensity, namely, 10^{18} W/cm^2, the bulk electron density remains nearly constant, because no energetic electrons with relativistic kinetic energy are injected into the target to introduce any structural changes such as plasma oscillation and instabilities, and thus the structure factor is close to unity, $S(q) \simeq 1$. Therefore, the dependence of SAXS intensity caused by the preplasma expansion can be simplified as

$$I(q) \simeq I_0 \frac{1}{q^3} e^{-q^2\sigma^2}, \tag{3}$$

Figure 3 shows the experimentally measured SAXS patterns and lineouts normalized by the incident XFEL energy from 40 to 1.5 ps before the arrival of the ReLaX peak laser intensity. The hot shots shown in Figs. 3(g)–3(l) have been selected on the basis of a similarly high He$_\alpha$ yield, indicating similar laser absorption efficiency for each shot due to the spatial jitter of the ReLaX laser spot, of the order of the focal spot size. Before each hot shot pumped by the ReLaX laser, we took an XFEL-only reference for the cold target geometry and XFEL–target overlap, as shown in Figs. 3(a)–3(f). Cold wire scattering is seen to be consistent over the reference shots, both for the streaks in Figs. 3(a)–3(f) and for the lineouts in Fig. 3(m) over four orders of magnitude in signal, indicating uniform wire edge sharpness. Fitting the measured SAXS profile in Fig. 3(m) with Eq. (3) yields a scale length or roughness below 10 nm. The intensity on the right SAXS streak is stable from shot to shot. On the left streak, the intensity shows greater variation. This asymmetric scattering feature is likely caused by the XFEL spatial jitter and randomly distributed nanostructures on the wire surface. For the hot shots, the 2D streak

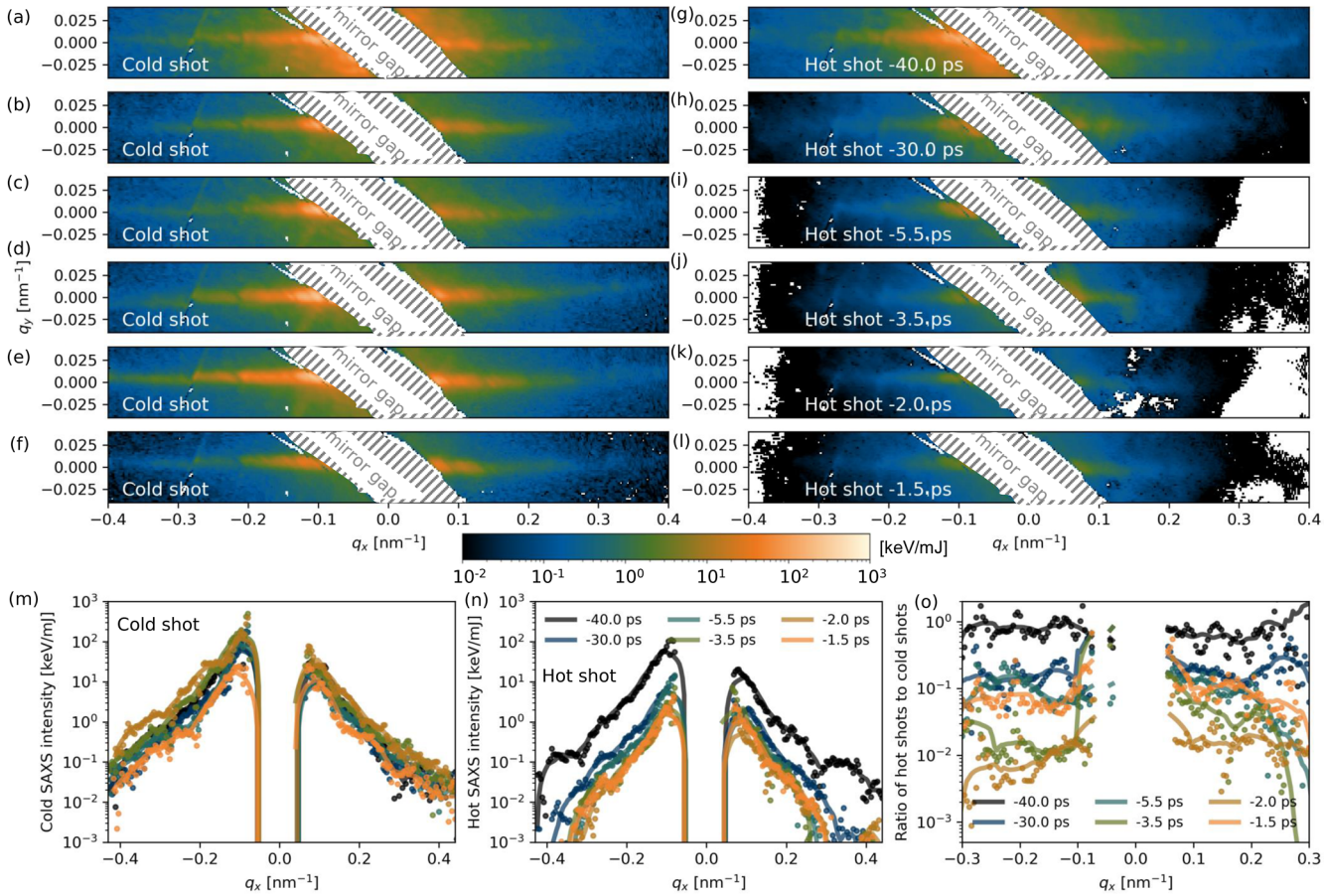

FIG. 3. Time-resolved SAXS patterns and horizontal lineouts through $q_y = 0$ averaged over ten pixels. The hot-shot SAXS patterns in (g)–(l) and the lineouts in (n) were taken during the rising slope of the ReLaX laser from 40 to 1.5 ps before the arrival of the peak pulse intensity. The corresponding cold-shot SAXS patterns in (a)–(e) and the lineouts in (m) were taken before each hot shot to provide an XFEL-only reference for the initial wire edge sharpness. Horizontal lineouts of the ratio of hot-shot to cold-shot SAXS intensity are shown in (o). The colorbar denotes the scattered X-ray energy normalized to the incoming XFEL energy.

SAXS patterns in Figs. 3(g)–3(l) and the outlines in Fig. 3(n) exhibit a clear trend of SAXS intensity decreasing with increasing time delay. To take account of the initial density edge, Fig. 3(o) shows the ratio of hot-shot to cold-shot SAXS intensity, which can be seen to exhibit the same decreasing trend, except for a time delay of −1.5 ps. It is surprising that the SAXS intensity decreases by one to two orders of magnitude from −40 to −1.5 ps within the entire measurable q range. Such a dramatic reduction in SAXS intensity is not observed in the case of sub-relativistic laser intensity.[24] It reveals that a pre-plasma is formed and expanded at least 30 ps (corresponding to an intensity of $\sim 5 \times 10^{13}$ W/cm^2) before the arrival of the main pulse with peak intensity 5×10^{20} W/cm^2. As well as the decrease in SAXS intensity, we also observe that the slope of the right streak becomes slightly steeper, which is correlated with the smoother edge caused

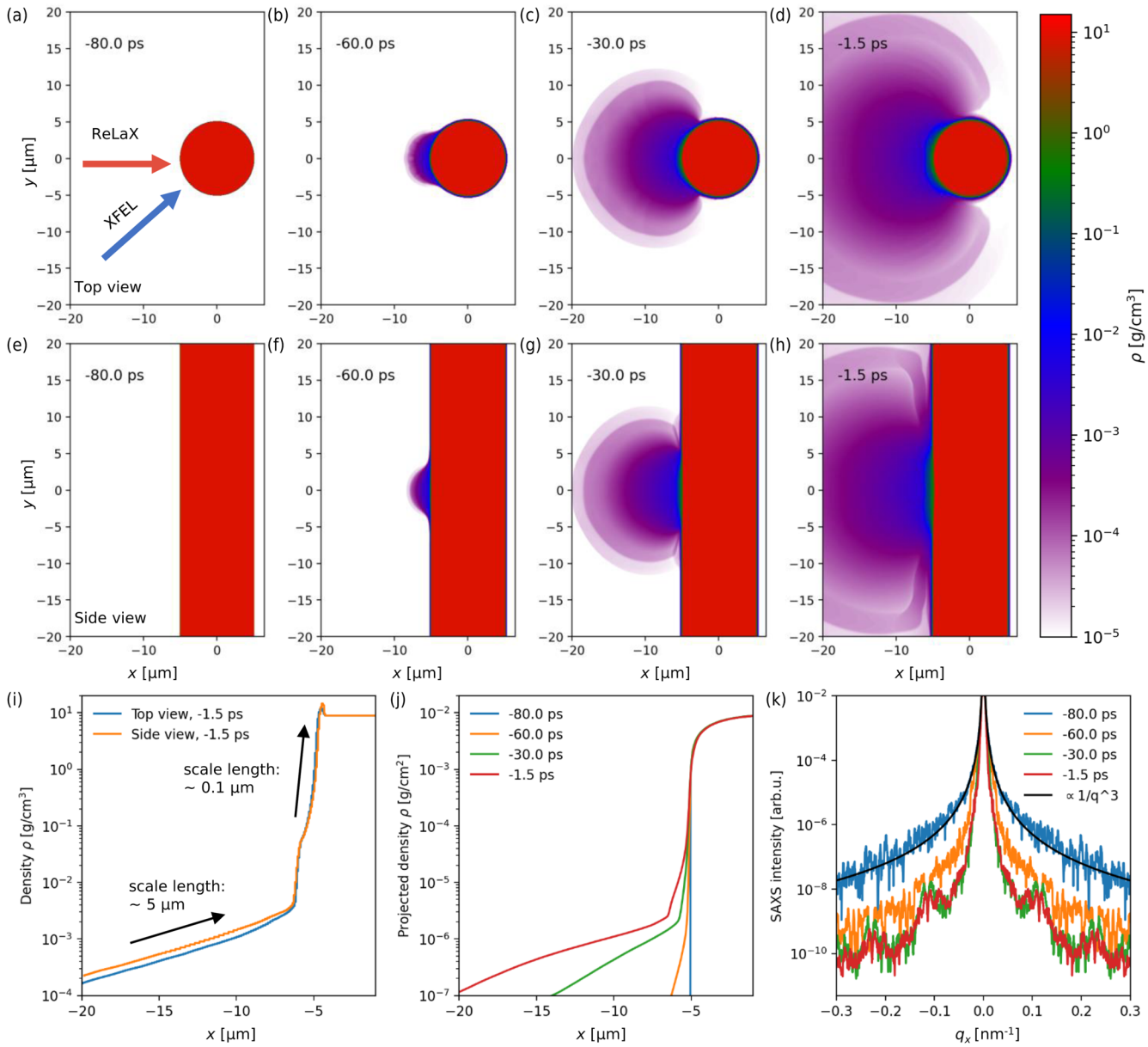

FIG. 4. 2D-MHD simulation results for the spatiotemporal evolution of Cu mass density following laser irradiation of a Cu wire target for (a)–(d) a circular geometry, corresponding to a top view of the target, and (e)–(h) a flat geometry, corresponding to a side view of the target. (i) Comparison of the central lineouts of the Cu mass density for the top- and side-view cases at −1.5 ps. (j) Temporal evolution of the projected density along the XFEL propagation direction and (k) the corresponding synthetic SAXS intensity.

by the pre-expansion. However, the slope of the left streak remains constant, which makes it unreliable to extract the scale length of the preplasma by fitting the SAXS data with Eq. (3). It implies that the dynamic density profile of the preplasma is complex and cannot be described simply by an error function.

To verify this scenario, we performed two-dimensional magnetohydrodynamic (2D-MHD) simulations of both the top view (circular geometry) and side view (flat geometry) of a wire target with the open-source FLASH code[48] to predict preplasma formation driven by the rising slope of the ReLaX laser pulse, from −80 to −1.5 ps before the arrival of the peak pulse. This corresponds to an increase in laser intensity from ~10^{12} to ~10^{16} W/cm^2, as shown in Fig. 1. All MHD simulations used the IONMIX equation of state (EOS) library.[49] The adaptive mesh size and time step were set to satisfy the Courant–Friedrichs–Lewy (CFL) conditions to ensure the convergence of the simulations. Figures 4(a)–4(d) and 4(e)–4(h) show the simulated spatiotemporal evolution of the Cu mass density for the top and side views of the wire target, respectively. It is evident that the initial sharp-edged density profile of the Cu wire is smoothed by the hydrodynamic expansion of the preplasma, resulting in different characteristic scale lengths. Up to 1.5 ps before the arrival of the peak laser intensity, the preplasma density profile exhibits a short scale length of ~100 nm near the initial solid target surface, extending into a much lower-density region with a longer scale length of ~5 μm in both cases, as shown in Fig. 4(i). Owing to momentum conservation, a thin compression layer of ~200 nm with a compression factor of ~1.6, driven by the prepulse, is also observed. The complex density profile does not follow an error function, preventing extraction of the preplasma scale length using Eq. (3) to fit the SAXS data. Alternatively, based on the projected density along the XFEL propagation direction, as shown in Fig. 4(j), forward SAXS calculations were performed using Eq. (1) for quantitative comparison with the experimental data. Figure 4(k) shows the temporal evolution of the synthetic SAXS signal, which exhibits a generally similar decreasing trend to the experimental measurements in Fig. 3. The initial SAXS intensity arising from the sharp surface nicely follows the expected wire form factor, $1/q^3$. As the preplasma expands, the SAXS intensity decreases rapidly until $t \approx -30$ ps, after which it remains nearly constant, indicating that the short scale length in the SAXS-sensitive region near solid density is preserved. At −1.5 ps, the SAXS intensity is nearly two orders of magnitude lower than in the cold case, in good agreement with the experimental data.

We notice that experimental shot-to-shot uncertainties such as the fine structure of the initial target surface, XFEL jitter, laser contrast fluctuations, and overlapping of the ReLaX laser, XFEL, and wire, can also influence the SAXS signal. At the arrival of the main laser pulse with relativistic intensity, the transport of fast electrons into the solid target can induce complex structural changes through the processes of hole boring,[24] plasma heating and ionization,[23] and oscillation and filamentation,[50] as inferred from our previous SAXS experiments. In this phase, the scattering features become much more complex, and we have to take into account the contribution of the structure factor $S(q)$. Additionally, the scattering intensity further decreases to near the noise level, making it challenging to extract reliable dynamic information. Accessing SAXS in the lower-q region will improve the data quality, which will be the subject of our follow-up experiments and analysis.

B. RXES measurements of heating and ionization dynamics

During the interaction between the ultra-short laser and the solid Cu with preformed plasma, a fraction of the electrons are accelerated to relativistic kinetic energy and transported into the solid, leading to subsequent ultra-fast bulk heating and collisional and pressure ionization. The ionization then empties the outer electron shells of the atoms, and opens the possibility of resonant X-ray absorption in an optical laser pump–XFEL probe experiment, namely, a transition from the K shell ($n = 1$) to a higher L ($n = 2$) or M ($n = 3$) shell, i.e., the inverse processes of K_α or K_β, as shown schematically in Fig. 5(a). For a given transition, for example

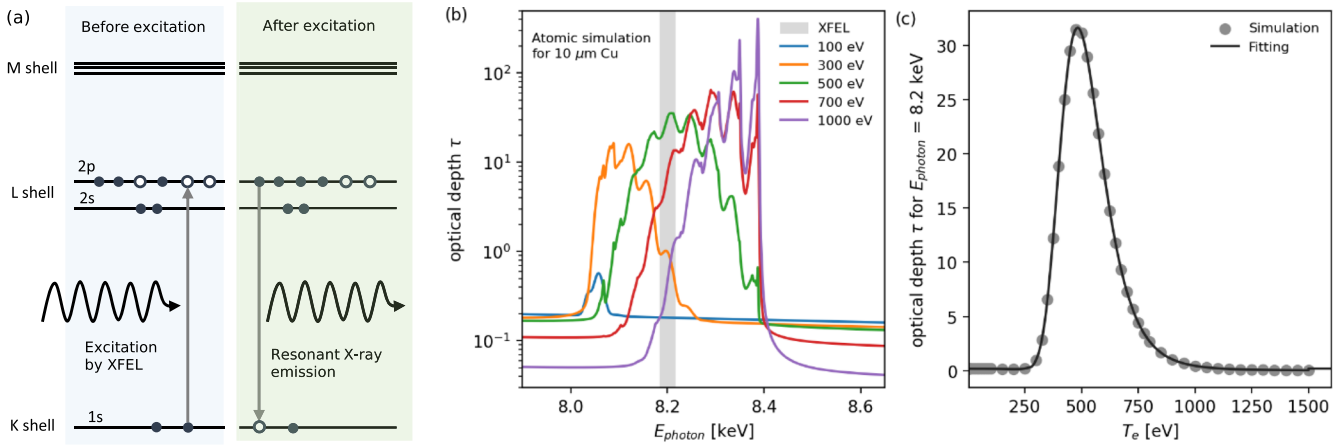

FIG. 5. (a) Schematic of electron excitation and resonant X-ray emission stimulated by an external XFEL. (b) Opacity spectra of a solid Cu plasma of 10 μm thickness at temperatures ranging from 100 to 1000 eV, calculated with the atomic code SCFLY. (c) Temperature dependence of Cu optical depth at the resonant photon energy of E_{photon} = 8.2 keV.

$1s \rightarrow 2p$, the binding energy depends on the number of remaining bound electrons. Owing to the screening effect of the nuclear Coulomb potential, the higher-charge state requires a higher transition energy or resonant X-ray photon energy. The scenario is clearly seen from the opacity spectra of a 10 μm solid-density Cu plasma simulated by the atomic collisional radiative code SCFLY,[51] as shown in Fig. 5(b). In the calculated opacity spectrum, one sees a distribution of several satellite, slightly overlapping, peaks. Each peak corresponds to a bound–bound transition for a specific charge state. It is well known that the transition energy of cold K_α of Cu is 8.0478 keV according to NIST data.[52] As the plasma temperature increases, the average charge state increases, and thus the transition energy or the peak position of the spectrum shifts to higher photon energy. On the basis of this principle, an XFEL can be used to resonantly pump a specific atomic transition and thus achieve enhanced X-ray emission. This method has also been successfully applied to generate highly coherent atomic X-ray lasers pumped by an XFEL.[53,54]

In our experiment, we tune the photon energy of XFEL at 8.2 keV, which is mostly in resonance with the bound–bound transition energy of the selected specific charge state of Cu ions, namely, Cu^{22+}. When the Cu is ionized to the particular charge state driven by the main laser pulse, the inner K-shell electrons will be resonantly excited by the XFEL photon to the higher L-shell electrons. These electrons then decay through a recombination process and re-emit photons at the same energy as the incident X rays, exciting them in a very short time and leading to an enhanced X-ray emission yield at the resonant energy. In the case that the solid-density plasma experiences continued heating, resulting in a higher ionization degree than the selected charge state, the plasma's opacity diminishes owing to the inability of bound electrons to establish a resonant transition channel. A reduction in opacity also occurs when the plasma undergoes a cooling process, as shown by the temperature-dependent opacity of the solid-density Cu plasma at the specific photon energy $E_{\text{photon}} = 8.2$ keV in Fig. 5(c).

Figure 6 shows the measured X-ray emission spectra for two cases: one with no resonant yield at ~0 ps and the other with a strong resonant yield at ~2.5 ps. Prominent peaks corresponding to the cold K_α transitions (8.02–8.04 keV) and the $2p \rightarrow 1s$ transitions in Cu^{26+} and Cu^{27+} (8.28–8.42 keV) are observed in both cases, indicating comparable initial interaction conditions. As these transitions do not interfere with the XFEL probe, their X-ray emission is

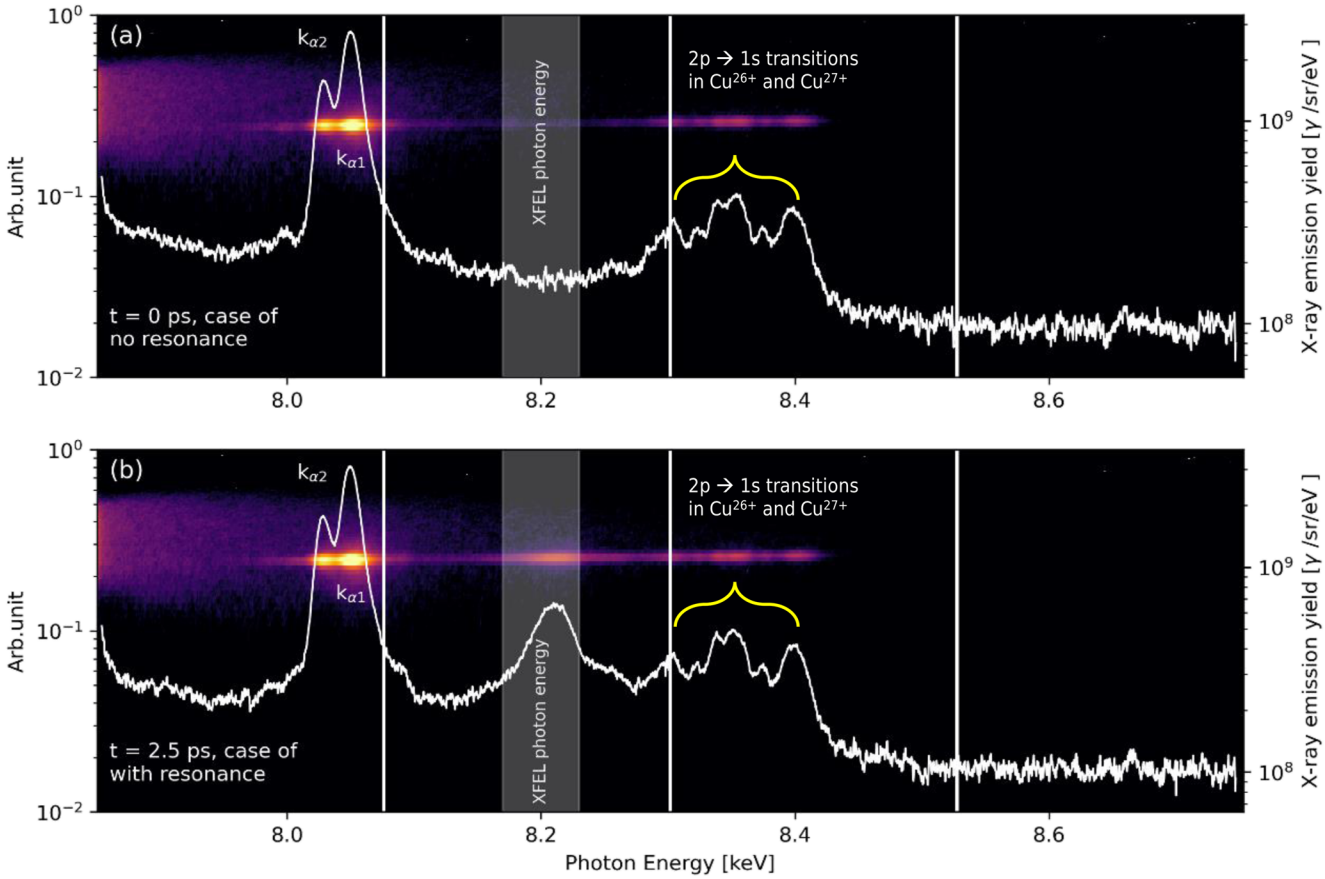

FIG. 6. Experimentally measured time-resolved X-ray emission spectra in (a) the case of no resonant yield at ~0 ps and (b) the case of strong resonant yield at ~2.5 ps. The gray shaded region indicates the photon energy range of the SASE XFEL beam, centered at 8.2 keV with a narrow bandwidth of ~40 eV, which is in resonance with the bound–bound transition of interest, $1s^2 2s^2 2p^3 \rightarrow 1s^1 2s^2 2p^4$. The white vertical lines represent the gap between two adjacent chips of the Jungfrau detector.

time-integrated over the entire duration of the laser–solid interaction. Here, the number of measured K_α photons is $\sim(8.5 \pm 0.7) \times 10^{10}$, which gives a total energy of ~1.36 mJ, assuming isotropic K_α emission. This yields a conversion efficiency of $\sim 4.2 \times 10^{-4}$ relative to the ReLaX laser energy. At ~0 ps when the Cu is not yet highly ionized, the spectrum shows that the spontaneous X-ray fluorescence within the energy window covered by the XFEL bandwidth is weak because of the rapid heating. Its intensity is insufficient to surpass the harsh bremsstrahlung environment background and thus is buried in the continuum radiation. In the case stimulated by the intense XFEL at 2.5 ps, the population of the specific transition state is significantly enhanced owing to the resonant absorption, leading to a distinct resonant peak well above the bremsstrahlung background, as shown in Fig. 6(b). The net yield of resonant X-ray emission is calculated to be $(1.5 \pm 0.5) \times 10^{10}$ photons/sr, which corresponds to (0.428 ± 0.08) mJ over the full solid angle. Given that the XFEL energy is measured to be ~0.787 mJ, the absorption efficiency in the strongly resonant case is approximately (54% ± 10%). By contrast, according to the Henke Tables,[55] the XFEL absorption in a cold Cu wire of 10 μm diameter is 22%. This finding is consistent with the results of the atomic simulation presented in Fig. 4(c), which show that the plasma opacity peaks at ~500 eV, leading to the strongest resonant X-ray emission and consequently the highest population of Cu^{22+} ions. Thus, measuring the temporal evolution of the resonant emission yield provides information on the temperature-dependent plasma opacity, or equivalently the XFEL attenuation. Following this principle, fitting the time-resolved emission spectra measured by RXES with simulated spectra allows extraction of the temperature, ionization, and recombination dynamics.

In conjunction with time-resolved spectroscopic measurements, resonant X-ray absorption imaging can be employed to further probe the spatial distribution of ionization within plasmas, as recently demonstrated in short-pulse laser-driven warm and hot dense matter experiments.[31,32,56] Such experiments significantly advance our understanding of electron transport in solid-density plasmas and hold substantial potential for improving the collisional and ionization models implemented in state-of-the-art PIC and MHD codes.[56]

C. XPCI measurements of shock-driven compression and expansion

Finally, we present the diagnostic results of Fresnel propagation-based X-ray phase-contrast imaging, which is sensitive to the density gradient at sub-micrometer scales, aiming to explore laser-driven blast waves in the interaction region and surface return current-driven cylindrical compression off the interaction point on timescales ranging from tens to hundreds of picoseconds. In contrast to the previous discussed diagnostics of SAXS and RXES with a ~10 μm XFEL field of view (FoV) on the 10 μm Cu wire, we switched the X-ray focusing scheme to have a ~30 μm FoV illuminating the target to record the interference between scattered and unscattered X rays. The X-ray focal point was calculated to be ~0.76 m in front of the sample with FWHM focal size ~1.7 μm. The X-ray imaging detector was positioned downstream at a distance $L = 6.31$ m from the sample plane. This led to an overall magnification $M = (6.31\ \text{m} + 0.76\ \text{m})/0.76\ \text{m} = 9.3$. The effective Fresnel number with respect to one pixel was then calculated as[28]

$$Fr_{\text{eff}} = \frac{\Delta x^2}{\lambda L M}, \tag{4}$$

with effective pixel size $\Delta x = 6.5\ \mu\text{m}/7.5 = 0.867\ \mu$m and X-ray wavelength $\lambda = 0.1512$ nm, giving $Fr_{\text{eff}} = 10^{-4}$.

Figure 7 shows the time-resolved XPCI images normalized by a synthetic X-ray flat field (X-ray illumination intensity) from 0 to 150 ps. For each delay, the synthetic flat field is computed on the basis of a principal component analysis (PCA) of a series of empty XFEL pulses post shot when the target has been totally destroyed by

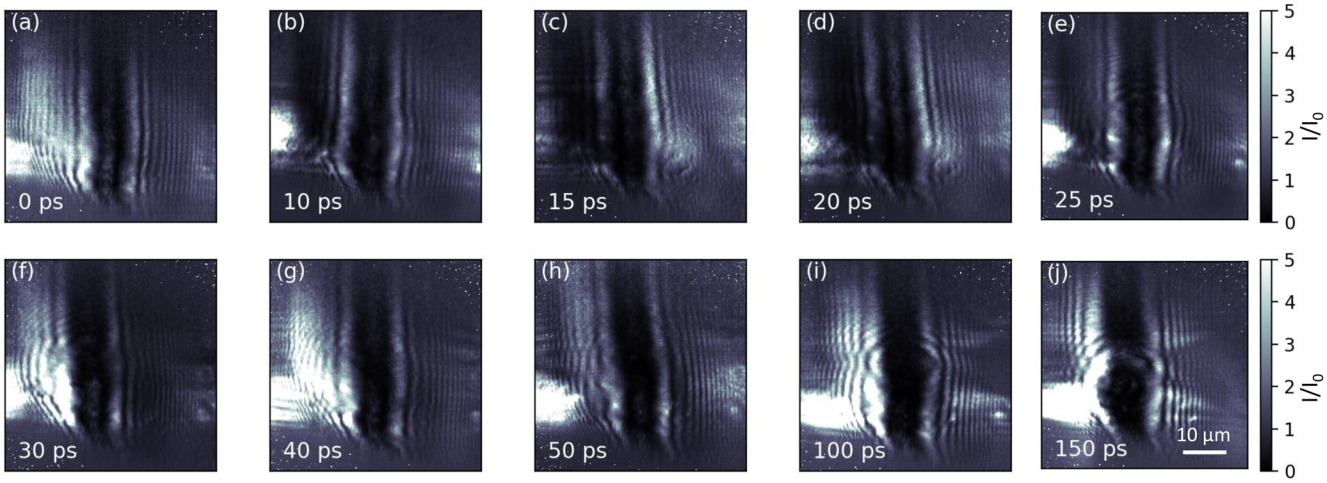

FIG. 7. Experimentally recorded time-resolved XPCI images normalized by a synthetic X-ray flat field from 0 ps (a) to 150 ps (j). Here, by changing the X-ray focusing scheme, the XFEL FoV has been switched from the ~10 μm used for SAXS and RXES diagnostics to ~30 μm illuminating the 10 μm Cu wire, thereby allowing interference between the scattered and freely propagated unscattered X rays. The scale bar applies to all panels.

the ReLaX laser.[28] Since the hot and post shots for each target occur in a short time window (~2 min), it is presumed that the principal components of the XFEL illumination field C_i remain unchanged. The PCA algorithm is then applied to solve a minimization problem. Given a measured intensity image Y (hot shot), we calculate the combination of weight factors w_i of the PCA components C_i that minimizes $|Y - \sum_i w_i C_i|$. This minimization can be approximated by the projection of Y onto the C_i, computed by a scalar product, which yields the w_i. With these steps, the synthetic flat field of each hot shot is computed. The whole algorithmic process has been thoroughly detailed in our previous work.[28]

In Fig. 7, we can clearly see the Fresnel fringes formed by interference between scattered and freely propagated unscattered X rays. The fringes exhibit axially asymmetric contrast on either side of the wire, owing to the XFEL spatial jitter and nonuniform distribution. The bright spots outside the primary beam and the twin fringes are artifacts caused by the nonideal beam shape and normalization algorithm. Nevertheless, the XPCI pattern varies significantly with the time delay. At 0 ps, the interference fringes remain nearly straight, indicating that there has been no significant target deformation due to hydrodynamic expansion and compression. As the time delay increases, the fringes progressively exhibit a greater degree of curvature, indicating target deformation due to the hole-boring process caused by the laser-driven blast wave at the interaction point. Such a hole-boring process was also evident from the tilted SAXS signal of the scattering surface in our previous work.[24] At 150 ps, the XPCI pattern is altered significantly, showing a nearly circular curvature with distinct expanding features, indicating the wire target is partially destroyed. Furthermore, the curved fringes observed outside the primary beam region suggest wire surface ablation which can cause surface compression and expansion induced by the heating of flowing return current.[15]

To precisely retrieve the key plasma parameters such as density and temperature, the ideal approach is to reconstruct the attenuation and phase-shift maps of the XFEL beam crossing the wire in real space that are encoded by the contrast fringes of the X-ray imaging shown in Fig. 7. Here, phase retrieval is performed using the efficient iterative algorithm of alternating projections,[28] enabling reconstruction of the phase shift maps as shown in Fig. 8. The phase shift is then expected to be proportional to the projected density along the XFEL beam path.[57] As we can see, the initial profile of the 10 μm Cu wire at 0 ps is clearly outlined, and is yet to be deformed by the intense laser pulse. At 150 ps, the laser-driven blast wave traverses radially through the entire thin wire and breaks out at the rear surface while continues to propagate transversely. The average velocity of the blast wave is estimated to be faster than 67 km/s, which is in agreement with the observation of direct X-ray imaging of a 25 μm Cu wire irradiated by the same ReLaX laser.[30] On the basis of the theoretical prediction $v_{\mathrm{shock}}^{\mathrm{thermal}} = \sqrt{3P/\rho_0}$, where ρ_0 is the initial mass density of Cu,[58] the thermal pressure of the blast wave is higher than 150 Mbar in the interaction region. Furthermore, the slight expansion of the wire profile away from the interaction point indicates plasma ablation, which could be driven by surface return current heating. This phenomenon is associated with cylindrical compression propagating toward the wire core, as predicted and more clearly observed in our recent direct X-ray imaging results, achieved by placing a focusing compound refractive lens stack between the target and the detector.[15,30] The limited visibility of blast wave and compression features in the reconstructed phase maps shown here is primarily due to the raw data quality, as well as uncertainties in propagation distances and artifacts in the flat-fielded XPCI, such as beam-clipping effects indicated by bright spots outside the primary beam in Fig. 7. For the other pump–probe delays, even after considerable tuning of the reconstruction parameters, the

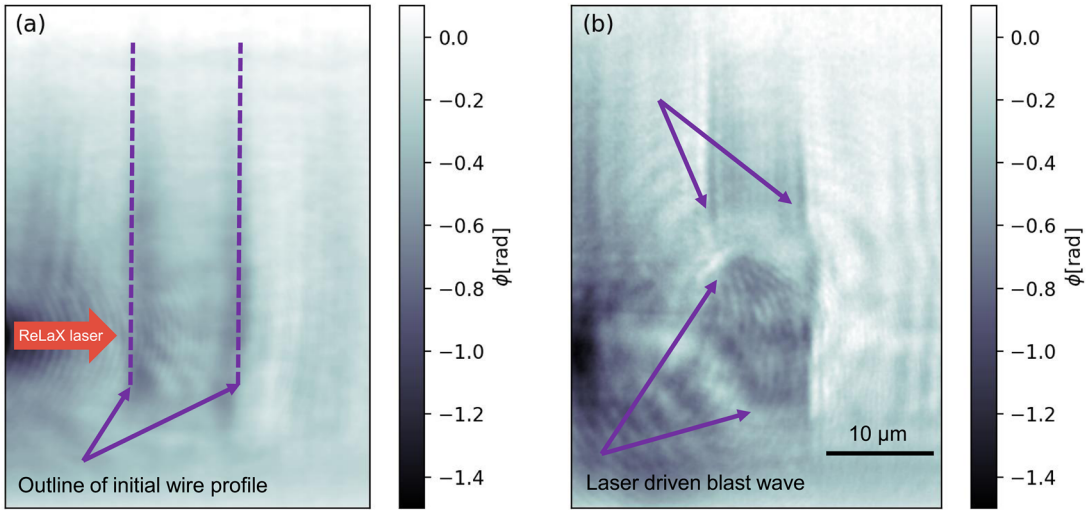

FIG. 8. Reconstructed phase maps from XPCI measurements at 0 ps (a) and 150 ps (b). Note that the distances from the focus to the wire and from the focus to the detector are set at 0.1 and 5.367 m, respectively, to achieve better reconstruction quality compared with the use of the nominal propagation parameters.

evolution of the aforementioned features does not show the expected reliability.

Alternatively, we could simulate the forward synthetic XPCI imaging using the Fresnel diffraction integral formula[59] to best fit the experimental measurements:

$$E(x,y,z) = \frac{1}{i\lambda}\iint_{-\infty}^{\infty} E(x',y',0)\frac{e^{ikr}}{r}\frac{z}{r}\,dx'\,dy', \tag{5}$$

where $r = \sqrt{(x-x')^2 + (y-y')^2 + z^2}$, i is the imaginary unit, k is the wavenumber, and $E(x',y',0)$ is the electric field of the X ray just as it exits the target plane. Such forward imaging simulations require inputs of density, opacity, and heating depth, which are typically predicted through a combination of PIC and MHD, or hybrid simulations, and are therefore highly model-dependent. This will be investigated in a follow-up study, since it is beyond the scope of the present demonstration.

Besides investigating shock and pinch physics, we also aimed to probe density modulations arising from the seeding and growth of kinetic and hydrodynamic instabilities using propagation-based XPCI. However, such phenomena have not been observed here, probably because of limitations in imaging resolution. Employing the seeding mode of the XFEL with a narrower bandwidth and nanofocused beam with a higher geometric magnification could improve the imaging resolution and quality for this purpose.[27] It should also be noted that although the direct X-ray imaging setup[30] provides intuitive and straightforward observations of laser-driven blast waves and transient surface return current-induced compression, offering a clear advantage over the phase retrieval results from XPCI in this setup, its phase reconstruction could suffer from phase errors caused by fabrication imperfections and debris in the imaging CRL stack placed between the sample and detector.[60] Additionally, direct X-ray imaging is limited in its application to low-density samples, owing to constraints of absorption contrast. These limitations could be addressed by the newly commissioned Talbot X-ray imaging technique at the XFEL facility, which incorporates an additional Talbot grating into the direct X-ray imaging setup.[61]

IV. CONCLUSIONS

We have successfully demonstrated the capability of capturing the multiscale spatiotemporal dynamics of electron transport on a nanometer to sub-micrometer spatial scale and a sub-picosecond to hundreds of picoseconds timescale, in a hot solid-density plasma created by an optical relativistic 3 J/30 fs/100 TW laser. This has been achieved using a high-brightness XFEL on the novel pump–probe platform at the European XFEL-HED station. By simultaneously employing multiple X-ray diagnostics of SAXS, XPCI, and RXES, we have been able to probe the preplasma expansion driven by the leading edge of the relativistic laser pulse, the ultra-fast heating and ionization dynamics at the arrival of the main pulse, and the hydrodynamic evolution to 150 ps after the laser–wire interaction. The decreasing trend of edge streak SAXS intensity sensitive to structural changes on a few-nanometer scale reveals that the preplasma is formed and expands at least 30 ps (corresponding to an intensity of $\sim 5 \times 10^{13}$ W/cm^2) before the arrival of the peak pulse. A forward SAXS calculation based on the MHD-simulated preplasma density profile, which exhibits a short ~100 nm scale length near the solid target surface, is in good agreement with the experimental data. Furthermore, we have presented time-resolved RXES measurements, achieved by resonantly XFEL pumping a specific charge state in ReLaX laser-driven hot dense Cu plasmas. The intensity of the resonant X-ray emission directly reflects the population of the corresponding ionic charge state Cu^{22+}, thereby providing valuable insights into the temporal evolution of heating, ionization, and recombination dynamics. Finally, we have presented the temporal evolution of XPCI measurements and the corresponding phase reconstruction results, which reveal the hydrodynamic expansion and compression induced by shock waves originating from direct laser ablation and transient surface return currents sensitive to the sub-micrometer-scale density gradients. Further improvements to the experimental capability, such as accessing the lower SAXS regime, implementing resonant absorption imaging, and utilizing Talbot X-ray imaging, have also been proposed. Note that although the experimental capabilities of the novel combination of advanced X-ray diagnostics—including SAXS, XPCI, and RXES—have been demonstrated on high-power laser-driven wire targets, these diagnostics are universal and can also be applied to other geometries to study kinetic instabilities,[50] target expansion,[22] and shock evolution. Nevertheless, owing to the sensitivity of beam pointing caused by the limited surface area of the wire target, the initial laser–target coupling conditions—such as ReLaX and XFEL pointing and overlap affected by natural beam jitter—can be post-analyzed using secondary emission yields and X-ray imaging.[56] These advantages make the wire target particularly well suited to maximize the capabilities of HED facilities.

To the best of our knowledge, this work constitutes the first comprehensive investigation of complex solid-density plasma dynamics throughout the entire process of relativistic laser–solid interactions in a single experiment, enabled by the unprecedented probing capabilities of the XFEL. These findings offer a valuable experimental benchmark for PIC and MHD simulations, which are widely employed in the high-energy-density physics community. The results are also beneficial to advanced applications of laser–plasma-based particle acceleration and the creation of high-energy-density matter, and could provide useful insights for planetary science, astrophysics, and fusion energy research.

ACKNOWLEDGMENTS

We acknowledge the European XFEL in Schenefeld, Germany, for the provision of X-ray free-electron laser beamtime at HED SASE2 under Proposal No. 3129 and would like to thank the staff for their assistance. We are indebted to the HIBEF User Consortium for the provision of instrumentation and staff that enabled this experiment. We gratefully acknowledge Professor O. Rosmej, Dr. J. F. Ong, Dr. A. Hirsch-Passicos, and C. Qu for valuable discussions. We would also like to thank the HZDR and DESY HPC group for their assistance on the high-performance computational clusters. The FLASH code used in this work was developed in part by the DOE NNSA- and DOE Office of Sciences-supported Flash Center for Computational Science at the University of Chicago and the University of Rochester. T. Engler acknowledges funding from Grant No. HIDSS-0002 DASHH (Data Science in Hamburg—Helmholtz Graduate School for the Structure of Matter). This work was partially

supported by the Helmholtz Imaging platform through the project "SmartPhase."

AUTHOR DECLARATIONS

Conflict of Interest

The authors have no conflicts to disclose.

Author Contributions

L.H. lead the experiment. L.H., M.S., A.L.G., T.K., M.M., T.P., H.P.S., T.T., U.Z., and T.E.C. conceived the experimental setup. L.H., M.S., L.Y., T.E., X.P., C.B., E.B., A.L.G., S.G., M.H., H.H., M.K., W.L., M.M., M.N., M.O., Ö.Ö., A.P., T.P., L.R., M.R., H.P.S., J.P.S., M.T., T.T., and T.E.C. performed the experiment. L.H., M.S., L.Y., O.H., J.H., T.E., X.P., Y.C., T.K., R.A., E.E., A.L.G., P.H., T.P., S.S., E.T., T.T., U.Z., and T.E.C. analyzed the data. L.H. wrote the original draft of the manuscript. All authors discussed the results and revised the manuscript.

Lingen Huang: Conceptualization (lead); Data curation (lead); Formal analysis (lead); Investigation (lead); Methodology (lead); Visualization (lead); Writing – original draft (lead); Writing – review & editing (lead). **Michal Šmíd**: Conceptualization (lead); Formal analysis (equal); Methodology (equal); Writing – review & editing (equal). **Long Yang**: Formal analysis (equal); Investigation (equal); Visualization (equal); Writing – review & editing (equal). **Oliver Humphries**: Formal analysis (equal); Investigation (equal); Writing – review & editing (equal). **Johannes Hagemann**: Formal analysis (equal); Methodology (equal); Writing – review & editing (equal). **Thea Engler**: Formal analysis (equal); Methodology (equal); Writing – review & editing (equal). **Xiayun Pan**: Formal analysis (equal); Methodology (equal); Writing – review & editing (equal). **Yangzhe Cui**: Formal analysis (equal); Writing – review & editing (equal). **Thomas Kluge**: Conceptualization (lead); Formal analysis (equal); Investigation (equal); Writing – review & editing (equal). **Ritz Aguilar**: Formal analysis (equal); Investigation (equal); Writing – review & editing (equal). **Carsten Baehtz**: Investigation (equal); Writing – review & editing (equal). **Erik Brambrink**: Investigation (equal); Writing – review & editing (equal). **Engin Eren**: Formal analysis (equal); Investigation (equal); Writing – review & editing (equal). **Katerina Falk**: Investigation (equal); Writing – review & editing (equal). **Alejandro Laso Garcia**: Conceptualization (lead); Formal analysis (equal); Investigation (equal); Writing – review & editing (equal). **Sebastian Göde**: Investigation (equal); Writing – review & editing (equal). **Christian Gutt**: Investigation (equal); Writing – review & editing (equal). **Mohamed Hassan**: Investigation (equal); Writing – review & editing (equal). **Philipp Heuser**: Formal analysis (equal); Writing – review & editing (equal). **Hauke Höppner**: Investigation (equal); Writing – review & editing (equal). **Michaela Kozlova**: Investigation (equal); Writing – review & editing (equal). **Wei Lu**: Formal analysis (equal); Writing – review & editing (equal). **Josefine Metzkes-Ng**: Investigation (equal); Writing – review & editing (equal). **Masruri Masruri**: Investigation (equal); Writing – review & editing (equal). **Mikhail Mishchenko**: Conceptualization (lead); Investigation (equal); Writing – review & editing (equal). **Motoaki Nakatsutsumi**: Investigation (equal); Writing – review & editing (equal). **Masato Ota**: Investigation (equal); Writing – review & editing (equal). **Özgül Öztürk**: Investigation (equal); Writing – review & editing (equal). **Alexander Pelka**: Investigation (equal); Writing – review & editing (equal). **Irene Prencipe**: Investigation (equal); Writing – review & editing (equal). **Thomas R. Preston**: Conceptualization (lead); Investigation (equal); Writing – review & editing (equal). **Lisa Randolph**: Investigation (equal); Writing – review & editing (equal). **Martin Rehwald**: Investigation (equal); Writing – review & editing (equal). **Hans-Peter Schlenvoigt**: Conceptualization (lead); Investigation (equal); Writing – review & editing (equal). **Ulrich Schramm**: Investigation (equal); Writing – review & editing (equal). **Jan-Patrick Schwinkendorf**: Investigation (equal); Writing – review & editing (equal). **Sebastian Starke**: Formal analysis (equal); Investigation (equal); Writing – review & editing (equal). **Radka Štefaníková**: Investigation (equal); Writing – review & editing (equal). **Erik Thiessenhusen**: Formal analysis (equal); Investigation (equal); Writing – review & editing (equal). **Monika Toncian**: Investigation (equal); Writing – review & editing (equal). **Toma Toncian**: Conceptualization (lead); Investigation (equal); Writing – review & editing (equal). **Jan Vorberger**: Investigation (equal); Writing – review & editing (equal). **Ulf Zastrau**: Conceptualization (lead); Investigation (equal); Writing – review & editing (equal). **Karl Zeil**: Investigation (equal); Writing – review & editing (equal). **Thomas E. Cowan**: Conceptualization (lead); Formal analysis (equal); Investigation (equal); Methodology (equal); Writing – review & editing (equal).

DATA AVAILABILITY

The data that support the findings of this study are available from the corresponding author upon reasonable request.[62]

REFERENCES

[1] L. G. Huang, T. Kluge, and T. E. Cowan, "Dynamics of bulk electron heating and ionization in solid density plasmas driven by ultra-short relativistic laser pulses," Phys. Plasmas **23**, 063112 (2016).

[2] V. Bagnoud, J. Hornung, T. Schlegel, B. Zielbauer, C. Brabetz *et al.*, "Studying the dynamics of relativistic laser-plasma interaction on thin foils by means of Fourier-transform spectral interferometry," Phys. Rev. Lett. **118**, 255003 (2017).

[3] C. Bernert, S. Assenbaum, S. Bock, F.-E. Brack, T. E. Cowan *et al.*, "Transient laser-induced breakdown of dielectrics in ultrarelativistic laser-solid interactions," Phys. Rev. Appl. **19**, 014070 (2023).

[4] S. C. Wilks, W. L. Kruer, M. Tabak, and A. B. Langdon, "Absorption of ultra-intense laser pulses," Phys. Rev. Lett. **69**, 1383 (1992).

[5] F. N. Beg, A. R. Bell, A. E. Dangor, C. N. Danson, A. P. Fews *et al.*, "A study of picosecond laser–solid interactions up to 10^{19} W/cm^{-2}," Phys. Plasmas **4**, 447 (1997).

[6] T. Kluge, T. Cowan, A. Debus, U. Schramm, K. Zeil *et al.*, "Electron temperature scaling in laser interaction with solids," Phys. Rev. Lett. **107**, 205003 (2011).

[7] J. Park, R. Tommasini, R. Shepherd, R. A. London, C. Bargsten *et al.*, "Absolute laser energy absorption measurement of relativistic 0.7 ps laser pulses in nanowire arrays," Phys. Plasmas **28**, 023302 (2021).

[8] C. Bernert, S. Assenbaum, F.-E. Brack, T. E. Cowan, C. B. Curry *et al.*, "Off-harmonic optical probing of high intensity laser plasma expansion dynamics in solid density hydrogen jets," Sci. Rep. **12**, 7287 (2022).

[9] K. Quinn, P. A. Wilson, C. A. Cecchetti, B. Ramakrishna, L. Romagnani *et al.*, "Laser-driven ultrafast field propagation on solid surfaces," Phys. Rev. Lett. **102**, 194801 (2009).

[10]K. Quinn, L. Romagnani, B. Ramakrishna, G. Sarri, M. E. Dieckmann *et al.*, "Weibel-induced filamentation during an ultrafast laser-driven plasma expansion," Phys. Rev. Lett. **108**, 135001 (2012).
[11]A. Morace, L. Fedeli, D. Batani, S. Baton, F. N. Beg *et al.*, "Development of x-ray radiography for high energy density physics," Phys. Plasmas **21**, 102712 (2014).
[12]U. Zastrau, P. Audebert, V. Bernshtam, E. Brambrink, T. Kämpfer *et al.*, "Temperature and *kα*-yield radial distributions in laser-produced solid-density plasmas imaged with ultrahigh-resolution x-ray spectroscopy," Phys. Rev. E **81**, 026406 (2010).
[13]S. H. Glenzer and R. Redmer, "X-ray Thomson scattering in high energy density plasmas," Rev. Mod. Phys. **81**, 1625 (2009).
[14]L. G. Huang, H. P. Schlenvoigt, H. Takabe, and T. E. Cowan, "Ionization and reflux dependence of magnetic instability generation and probing inside laser-irradiated solid thin foils," Phys. Plasmas **24**, 103115 (2017).
[15]L. Yang, M. Rehwald, T. Kluge, A. Laso Garcia, T. Toncian *et al.*, "Dynamic convergent shock compression initiated by return current in high-intensity laser–solid interactions," Matter Radiat. Extremes **9**, 047204 (2024).
[16]F. Kroll, F.-E. Brack, C. Bernert, S. Bock, E. Bodenstein *et al.*, "Tumour irradiation in mice with a laser-accelerated proton beam," Nat. Phys. **18**, 316 (2022).
[17]J. Nuckolls, L. Wood, A. Thiessen, and G. Zimmerman, "Laser compression of matter to super-high densities: Thermonuclear (CTR) applications," Nature **239**, 139 (1972).
[18]R. Kodama, P. A. Norreys, K. Mima, A. E. Dangor, R. G. Evans *et al.*, "Fast heating of ultrahigh-density plasma as a step towards laser fusion ignition," Nature **412**, 798 (2001).
[19]U. Zastrau, K. Appel, C. Baehtz, O. Baehr, L. Batchelor *et al.*, "The high energy density scientific instrument at the european XFEL," J. Synchrotron Radiat. **28**, 1393 (2021).
[20]B. Nagler, B. Arnold, G. Bouchard, R. F. Boyce, R. M. Boyce *et al.*, "The matter in extreme conditions instrument at the linac coherent light source," J. Synchrotron Radiat. **22**, 520 (2015).
[21]T. Yabuuchi, A. Kon, Y. Inubushi, T. Togahi, K. Sueda *et al.*, "An experimental platform using high-power, high-intensity optical lasers with the hard x-ray free-electron laser at SACLA," J. Synchrotron Radiat. **26**, 585 (2019).
[22]T. Kluge, M. Rödel, J. Metzkes-Ng, A. Pelka, A. L. Garcia *et al.*, "Observation of ultrafast solid-density plasma dynamics using femtosecond x-ray pulses from a free-electron laser," Phys. Rev. X **8**, 031068 (2018).
[23]L. Gaus, L. Bischoff, M. Bussmann, E. Cunningham, C. B. Curry *et al.*, "Probing ultrafast laser plasma processes inside solids with resonant small-angle x-ray scattering," Phys. Rev. Res. **3**, 043194 (2021).
[24]T. Kluge, M. Bussmann, E. Galtier, S. Glenzer, J. Grenzer *et al.*, "Probing shock dynamics inside micro-wire targets after high-intensity laser irradiation using small angle x-ray scattering of a free-electron laser," New J. Phys. **25**, 103036 (2023).
[25]L. Randolph, M. Banjafar, T. R. Preston, T. Yabuuchi, M. Makita *et al.*, "Nanoscale subsurface dynamics of solids upon high-intensity femtosecond laser irradiation observed by grazing-incidence x-ray scattering," Phys. Rev. Res. **4**, 033038 (2022).
[26]L. Randolph, M. Banjafar, T. Yabuuchi, C. Baehtz, M. Bussmann *et al.*, "(sub-) picosecond surface correlations of femtosecond laser excited al-coated multilayers observed by grazing-incidence x-ray scattering," Nanomaterials **14**, 1050 (2024).
[27]A. Schropp, R. Hoppe, V. Meier, J. Patommel, F. Seiboth *et al.*, "Imaging shock waves in diamond with both high temporal and spatial resolution at an XFEL," Sci. Rep. **5**, 11089 (2015).
[28]J. Hagemann, M. Vassholz, H. Hoeppe, M. Osterhoff, J. M. Rosselló *et al.*, "Single-pulse phase-contrast imaging at free-electron lasers in the hard X-ray regime," J. Synchrotron Radiat. **28**, 52 (2021).
[29]D. S. Hodge, A. F. T. Leong, S. Pandolfi, K. Kurzer-Ogul, D. S. Montgomery *et al.*, "Multi-frame, ultrafast, x-ray microscope for imaging shockwave dynamics," Opt. Express **30**, 38405 (2022).
[30]A. Laso Garcia, L. Yang, V. Bouffetier, K. Appel, C. Baehtz *et al.*, "Cylindrical compression of thin wires by irradiation with a joule-class short-pulse laser," Nat. Commun. **15**, 7896 (2024).
[31]H. Sawada, T. Yabuuchi, N. Higashi, T. Iwasaki, K. Kawasaki *et al.*, "Ultrafast time-resolved 2D imaging of laser-driven fast electron transport in solid density matter using an x-ray free electron laser," Rev. Sci. Instrum. **94**, 033511 (2023).
[32]H. Sawada, T. Yabuuchi, N. Higashi, T. Iwasaki, K. Kawasaki *et al.*, "Spatiotemporal dynamics of fast electron heating in solid-density matter via xfel," Nat. Commun. **15**, 7528 (2024).
[33]S. Frydrych, J. Vorberger, N. J. Hartley, A. K. Schuster, K. Ramakrishna *et al.*, "Demonstration of x-ray Thomson scattering as diagnostics for miscibility in warm dense matter," Nat. Commun. **11**, 2620 (2020).
[34]N. F. Beier, H. Allison, P. Efthimion, K. A. Flippo, L. Gao *et al.*, "Homogeneous, micron-scale high-energy-density matter generated by relativistic laser-solid interactions," Phys. Rev. Lett. **129**, 135001 (2022).
[35]O. S. Humphries, P. Allan, C. R. D. Brown, L. M. R. Hobbs, S. F. James *et al.*, "Time evolution of transient plasma states from nanowire arrays irradiated at relativistic intensities," Commun. Phys. **3**, 170 (2020).
[36]M. Osterhoff, M. Vassholz, H. P. Hoeppe, J. M. Rosselló, R. Mettin *et al.*, "Nanosecond timing and synchronization scheme for holographic pump–probe studies at the MID instrument at European XFEL," J. Synchrotron Radiat. **28**, 987 (2021).
[37]T. Kluge, M. Bussmann, H.-K. Chung, C. Gutt, L. G. Huang *et al.*, "Nanoscale femtosecond imaging of transient hot solid density plasmas with elemental and charge state sensitivity using resonant coherent diffraction," Phys. Plasmas **23**, 033103 (2016).
[38]A. Laso Garcia, H. Höppner, A. Pelka, C. Bähtz, E. Brambrink *et al.*, "ReLaX: The Helmholtz international beamline for extreme fields high-intensity short-pulse laser driver for relativistic laser–matter interaction and strong-field science using the high energy density instrument at the European x-ray free electron laser facility," High Power Laser Sci. Eng. **9**, e59 (2021).
[39]N. Kujala, W. Freund, J. Liu, A. Koch, T. Falk *et al.*, "Hard x-ray single-shot spectrometer at the European x-ray free-electron laser," Rev. Sci. Instrum. **91**, 103101 (2020).
[40]T. R. Preston, S. Göde, J.-P. Schwinkendorf, K. Appel, E. Brambrink *et al.*, "Design and performance characterisation of the HAPG von Hámos spectrometer at the high energy density instrument of the European XFEL," J. Instrum. **15**, P11033 (2020).
[41]A. Mozzanica, M. Andrä, R. Barten, A. Bergamaschi, S. Chiriotti *et al.*, "The JUNGFRAU detector for applications at synchrotron light sources and XFELs," Synchrotron Radiat. News **31**, 16 (2018).
[42]M. Šmíd, C. Baehtz, A. Pelka, A. Laso García, S. Göde *et al.*, "Mirror to measure small angle x-ray scattering signal in high energy density experiments," Rev. Sci. Instrum. **91**, 123501 (2020).
[43]H. J. Kirkwood, R. Letrun, T. Tanikawa, J. Liu, M. Nakatsutsumi *et al.*, "Initial observations of the femtosecond timing jitter at the European XFEL," Opt Lett. **44**, 1650 (2019).
[44]J. Als-Nielsen and D. McMorrow, *Elements of Modern X-ray Physics* (John Wiley & Sons Ltd., New York, 2011), p. 434.
[45]T. Kluge, C. Gutt, L. G. Huang, J. Metzkes, U. Schramm *et al.*, "Using x-ray free-electron lasers for probing of complex interaction dynamics of ultra-intense lasers with solid matter," Phys. Plasmas **21**, 033110 (2014).
[46]G. Porod, "Small angle x-ray scattering," in *Proceedings of the Conference Held at Syracuse University* (Gordon and Breach, New York, 1956).
[47]M. Rödel, "Development of small-angle X-Ray scattering on a nanometer and femtosecond scale for the investigation of laser-driven matte," Ph.D. thesis, Technical University Dresden, 2022.
[48]B. Fryxell, K. Olson, P. Ricker, F. X. Timmes, M. Zingale *et al.*, "Flash: An adaptive mesh hydrodynamics code for modeling astrophysical thermonuclear flashes," Astrophys. J., Suppl. Ser. **131**, 273 (2000).
[49]J. J. Macfarlane, "IONMIX - A code for computing the equation of state and radiative properties of LTE and non-LTE plasmas," Comput. Phys. Commun. **56**, 259 (1989).
[50]P. Ordyna, C. Bähtz, E. Brambrink, M. Bussmann, A. Laso Garcia *et al.*, "Visualizing plasmons and ultrafast kinetic instabilities in laser-driven solids using x-ray scattering," Commun. Phys. **7**, 296 (2024).
[51]H.-K. Chung, M. H. Chen, and R. W. Lee, "Extension of atomic configuration sets of the non-LTE model in the application to the k_α diagnostics of hot dense matter," High Energy Density Phys. **3**, 57 (2007).

[52]A. Kramida, Y. Ralchenko, J. Reader, and NIST ASD Team, NIST Atomic Spectra Database (ver. 5.10), National Institute of Standards and Technology, Gaithersburg, MD, 2022, online available: https://physics.nist.gov/asd (31 January 2016).
[53]N. Rohringer, D. Ryan, R. A. London, M. Purvis, F. Albert *et al.*, "Atomic inner-shell x-ray laser at 1.46 nanometres pumped by an x-ray free-electron laser," Nature **481**, 488 (2012).
[54]H. Yoneda, Y. Inubushi, K. Nagamine, Y. Michine, H. Ohashi *et al.*, "Atomic inner-shell laser at 1.5-ångström wavelength pumped by an x-ray free-electron laser," Nature **524**, 446 (2015).
[55]B. L. Henke, E. M. Gullikson, and J. C. Davis, "X-ray interactions: Photoabsorption, scattering, transmission, and reflection at e = 50–30 000 ev, z = 1–92," At. Data Nucl. Data Tables **54**, 181 (1993).
[56]L. Huang, M. Mishchenko, M. Šmíd, O. Humphries, T. R. Preston *et al.*, "Probing ultrafast heating and ionization dynamics in solid density plasmas with time-resolved resonant x-ray absorption and emission," arXiv:2508.10627 (2025).
[57]D. S. Montgomery, "Invited article: X-ray phase contrast imaging in inertial confinement fusion and high energy density research," Rev. Sci. Instrum. **94**, 021103 (2023).
[58]J. J. Santos, B. Vauzour, M. Touati, L. Gremillet, J.-L. Feugeas *et al.*, "Isochoric heating and strong blast wave formation driven by fast electrons in solid-density targets," New J. Phys. **19**, 103005 (2017).
[59]J. W. Goodman, *Introduction to Fourier Optics* (Roberts and Company Publishers, 2015).
[60]R. Celestre, S. Berujon, T. Roth, M. Sanchez del Rio, and R. Barrett, "Modelling phase imperfections in compound refractive lenses," J. Synchrotron Radiat. **27**, 305 (2020).
[61]E. Galtier, H. J. Lee, D. Khaghani, N. Boiadjieva, P. McGehee *et al.*, "X-ray microscopy and talbot imaging with the matter in extreme conditions x-ray imager at LCLS," Sci. Rep. **15**, 7588 (2025).
[62]L. Huang and T. Kluge, Probing the lateral transport of hot electrons in relativistic laser solid wire target interactions, https://doi.org/10.22003/XFEL.EU-DATA-003129-00, 2022.